Full length article

Anisotropic strain: A critical role in domain evolution in (111)-Oriented ferroelectric films

M.J. Zou [a, b], Y.L. Tang [a], Y.L. Zhu [a, *], Y.P. Feng [a, c], Y.J. Wang [a], M.J. Han [a, c], N.B. Zhang [a, b], J.Y. Ma [a, b], B. Wu [a, b], X.L. Ma [a, d]

[a] Shenyang National Laboratory for Materials Science, Institute of Metal Research, Chinese Academy of Sciences, Wenhua Road 72, 110016, Shenyang, China
[b] School of Material Science and Engineering, University of Science and Technology of China, Hefei, 230026, China
[c] University of Chinese Academy of Sciences, Yuquan Road 19, 100049, Beijing, China
[d] State Key Lab of Advanced Processing and Recycling on Non-ferrous Metals, Lanzhou University of Technology, Langongping Road 287, 730050, Lanzhou, China

ARTICLE INFO

ABSTRACT

Domain behavior of (111)- oriented perovskite ferroelectric films is significantly different from (001)-/(101)- oriented ones, resulting in enhancing property responses such as a superior susceptibility and a reduced coercive field. However, the domain structures and evolutions with the thickness of (111)-oriented ferroelectric films, which are crucial to further understand the distinctive properties, are still obscure. In this study, the ferroelectric domains of (111)- oriented PbTiO$_3$ films are investigated by transmission electronic microscopy (TEM) and piezoresponse force microscopy (PFM). We identify the domain evolution with the film thicknesses under anisotropic strains imposed by the orthorhombic GdScO$_3$ (101)$_O$ substrates. Contrast analysis and electron diffraction patterns reveal that only four ferroelectric variants evolve in PTO films: d_2^+, d_2^-, d_3^+ and d_3^-, with the polarization directions along [010], [0$\bar{1}$0], [001] and [00$\bar{1}$], respectively. Two kinds of domain walls are formed: "inclined" (011) domain walls for d_2^-/d_3^+ (d_2^+/d_3^-) domains, "normal" (01$\bar{1}$) domain walls for d_2^-/d_3^+ (d_2^+/d_3^-) domains. The width of periodically distributed d_2^+/d_3^+ (d_2^-/d_3^-) domains increases with film thickness following the square root rule. Aberration-corrected scanning transmission electronic microscopy demonstrates the lattice characteristics of domains in (111)- oriented PbTiO$_3$ films are consistent with tetragonal ferroelectric domains. PFM studies reveal that both the out-of-plane and in-plane polarization components of d_2^-/d_3^+ (d_2^+/d_3^-) domains are non-identical, whereas the d_2^+/d_3^+ (d_2^-/d_3^-) domains possess uniform out-of-plane polarization component and non-uniform in-plane polarization component. This study discloses the domain structure in (111)- oriented tetragonal ferroelectric films under anisotropic strains and the association with the ferroelectric properties.

© 2019 Acta Materialia Inc. Published by Elsevier Ltd. All rights reserved.

1. Introduction

Ferroelectric materials have broad-application prospect in micro-electric devices, such as logic [1], nonvolatile memories [2], actuators [3], sensors [4] and ultrathin ferroelectric capacitors [5] for their switchable spontaneous polarizations and electromechanical coupling effects. A deep understanding and controlling of domain structure in ferroelectric films is crucial to promote the application of such materials. Recent progresses in (001)- oriented ferroelectric films have predicted and observed many kinds of possible domain structures, such as a/c domains, a_1/a_2 domains [6−9], flux-closure [10,11], vortex [12,13] and bubble domains [14]. Further studies have disclosed the domain architectures are usually influenced by epitaxial strain [15−17], film thickness [8,9], electrostatic boundary conditions [18−20] and other parameters [21]. In comparison with (001)- oriented ferroelectric films, the domain structure and behavior of (111)- oriented films are dramatically different, resulting in an increased domain density [22], an enhanced susceptibility [23] and a reduced coercive field [24]. A higher storage density, sensitivity, and power efficiency ferroelectric-based device can be fabricated based on such properties. However, unlike intensive studies on (001)- oriented

* Corresponding author.
E-mail address: ylzhu@imr.ac.cn (Y.L. Zhu).

ferroelectric films, the studies on (111)- oriented films are mainly focusing on macroscopic properties [22,24−26], especially lacking of structural characteristics of domains and domain walls at atomic scale.

A preliminary study on the domain structures suggested three domain variants d_1, d_2, and d_3 (without regard to ferroelectric polarization) for (111)- oriented ferroelectric tetragonal (F_T) films [27], where these domains were defined by their polar axis c (d_1 with c along [100], d_2 with c along [010] and d_3 with c along [001] direction). Each polar axis is related to two possible ferroelectric polarizations, thus there are six possible ferroelectric domains for (111)- oriented F_T films: d_1^+, $d_{\bar{1}}$, d_2^+, $d_{\bar{2}}$, d_3^+, $d_{\bar{3}}$. A later theoretical simulation demonstrated that the domain volume fraction keeps a constant as the misfit strain changes from compressive to tensile, unlike the dramatical change of domain volume fraction with the epitaxial misfit strain in (001)-/(101)- oriented films [23], but no experimental evidence comes out to support this prediction. In addition, PFM studies of (001)-, (101)- and (111)- oriented $PbZr_{0.2}Ti_{0.8}O_3$ films revealed that the density of domain walls of (111)- oriented films is much higher than the other two orientations, and the polarization reversal is completed by multi-step 90° switching, unlike 180° switching for (001)-/(101)- oriented films, which is confirmed by further molecular dynamics simulations [22]. The above results are based on that the (111)- oriented F_T films keep tetragonal as bulk. However, both theoretical and experimental works manifest that the crystal structure can be tuned by either epitaxial strains or film thickness. For example, both phenomenological Ginzburg-Landau-Devonshire thermodynamic model and density functional theory have revealed that the structure of (111)- oriented F_T films evolves from monoclinic phase to rhombohedral phase when the epitaxial strain changes from tensile to compressive [25,28,29]. Recent experimental studies have also revealed that the (111)- oriented $PbZr_{0.2}Ti_{0.8}O_3$ films exhibit a transition from tetragonal to monoclinic symmetry with decreasing film thickness [24]. It is important to point out that the results mentioned above are all based on isotropic strains applied to ferroelectric films. However, the crystallographic properties of (111)- oriented perovskite structure imply that the ferroelectric domain structures can also be tuned if we introduce different strain states along three orthorhombic <110>/<112> directions. Thus, to discover the domain evolution in (111)- oriented F_T films grown under anisotropic strain states would provide an effective strategy to craft ferroelectric domains, which is critical for designing future ferroelectric-based devices.

Here, we reveal that the domain variants of (111)- oriented $PbTiO_3$ (PTO) films are sensitive to both film thickness and anisotropic strains applied by the substrates. We use transmission electronic microscopy (TEM), piezoresponse force microscopy (PFM) and piezoresponse force spectroscopy (PFS) to study the domain structures of PTO films with different thicknesses epitaxially grown on $GdScO_3$ (GSO) (101)$_O$ substrates by pulsed laser deposition(PLD). TEM studies reveal that there are four ferroelectric variants evolving in the PTO films: d_2^+, $d_{\bar{2}}$, d_3^+ and $d_{\bar{3}}$, and two kinds of domain walls are formed: one is inclined domain walls lying on (011) along [01$\bar{1}$]$_{PC}$ ([010]$_O$) for d_2^+/d_3^+ ($d_{\bar{2}}/d_{\bar{3}}$) domains, the other is normal domain walls lying on (01$\bar{1}$) along [$\bar{2}$11]$_{PC}$ ([$\bar{1}$01]$_O$) for $d_{\bar{2}}/d_3^+$ ($d_2^+/d_{\bar{3}}$) domains, which is perpendicular to the former. The evolution is mainly controlled by the anisotropic strain and surface screening charges. The relationship between domain width and film thickness shows a good agreement with the well-established KMF's law (W $\propto d^{1/2}$). High resolution scanning transmission electronic microscopy (HR-STEM) study manifests that the lattice characteristics show a good agreement with tetragonal ferroelectric domains. PFM phase studies reveal that both the out-of-plane (OOP) and in-plane (IP) polarization components of $d_{\bar{2}}/d_3^+$ ($d_2^+/d_{\bar{3}}$)

domains are non-identical; in contrast, the d_2^+/d_3^+ ($d_{\bar{2}}/d_{\bar{3}}$) domains possess uniform OOP polarization components and non-uniform IP polarization components. Further PMS studies confirm the existence of d_2^+/d_3^+ and $d_{\bar{2}}/d_{\bar{3}}$ domains. These results are expected to provide help to further explore other (111) - oriented films with superior properties.

2. Experimental

Epitaxial thin films of PTO were grown on GSO (101)$_O$ substrates by pulsed laser deposition (PLD), using a Coherent ComPexPRO 201 KrF ($\lambda = 248$ nm) excimer laser. A sintered $PbTiO_3$ ceramic target (3mol% Pb-enriched) was applied. The target-substrate distance was 32 mm. For the growth of $PbTiO_3$, the temperature was kept at 700 °C, with the laser energy 2J cm^{-2}, a laser repetition rate of 4 Hz, and under an oxygen pressure 10Pa. Before deposition, all substrates were pre-heated to 800 °C to clean the substrate surface and then cooled down to the growth temperature (20 °C·min^{-1}). After deposition, the samples were annealed at the growth temperature in an oxygen pressure of $3*10^4$Pa, and then cooled down to room temperature at a cooling rate of 5 °C·min^{-1}.

Cross-sectional and plane-view samples were prepared by slicing, grinding, dimpling, and finally ion milling by using PIPS, while plane-view samples were milled only from the substrate side. The final ion milling voltage was less than 1 kV to reduce amorphous layer produced by ion beam damage, and the final milling angle is 5°. A JEOL 2100 transmission electron microscope was used for electron diffraction and diffraction contrast analysis. The HAADF-STEM image was acquired using Titan G^2 60−300 microscope with a high-brightness field-emission gun and double aberration (Cs) correctors from CEOS operating at 300 kV, while the beam convergence angle was 25 mrad and the collection angle ranged from 50 mrad to 250 mrad. Strain analysis were based on GPA, which was carried out using Gatan Digital Micrograph software. The nonlinear drift distortion in scanning probe images were corrected by using the algorithm described in literature [30].

The PFM studies were carried out on a CypherS (Oxford Instruments) using Ir/Pt-coated conductive tips and Pt−Si doping conductive tips. The former tips, which the radius of curvature is more than 20 nm, were used to characterize the domain structure of 90 nm PTO films, and the later (with a radius of curvature < 10 nm) were used to characterize the domain structure in 20 nm PTO films. The same Ir/Pt-coated conductive tips are used for PMS characterization.

3. Results and discussion

A serial of PTO films with different thickness were epitaxially grown on GSO (101)$_O$ substrates, that is (111) for a pseudo cubic coordinate system. All of the orientations marked below without subscripts represent pseudo cubic perovskite. The strain state between substrates and films is analyzed based on bulk value of GSO and PTO [31,32]. Figure S1 shows the atomic structure schematics of GSO substrates and d_1, d_2, and d_3 domains (without consideration of ferroelectric polarization) observed from [111] direction. There are three pairs of orthorhombic <110>/<112> directions in (111) plane as shown in Figure S1a. To compare the misfit strains between the three kinds of domains and substrate, the three pairs of in-plane lattice parameters are calculated according to the lattice constants of GSO and PTO [31,32]. The lattice mismatch between the film and substrate at room temperature can be calculated by the following equation [33]:

$$f = \frac{d(GSO) - d(PTO)}{d(GSO)}$$

The results are summarized in Table 1. Unlike cubic substrates, the in-plane lattice parameters along three orthorhombic <110>/<112> directions of GSO substrates are not uniform, resulting in anisotropic strains applied to the PTO films, which may play an important role in domain evolution in (111)- oriented ferroelectric tetragonal films. By further comparing the absolute magnitude of misfit strains between GSO substrates and $d_1/d_2/d_3$ domains, it can be deduced that only d_2/d_3 domains can exist in epitaxial PTO films grown on GSO $(101)_O$ substrates to minimize elastic energy since d_1 domains show relatively large misfit strains along certain direction such as 4.2% for $[01\bar{1}]$.

To have an overview of the domain structures in (111) oriented PTO films, a serial of plane-view TEM samples were prepared. Increasing the film thickness from 8 nm to 20 nm, 50 nm and finally 90 nm, the morphologies are displayed in Fig. 1a–d. It can be seen that stripe-like contrast exists in the four different thick PTO films. Usually, such contrast may come from ferroelectric domains, dislocations or regular distributed precipitates. The following selected area electron diffraction (SAED) and high resolution (HR) high angle annular dark field (HAADF) scanning transmission electronic microscopy (STEM) studies corroborate that the contrast mainly comes from ferroelectric domains in (111)- oriented PTO films. The dominant feature is that a mixed state (Fig. 1a and b) containing domain walls along $[01\bar{1}]$ and $[\bar{2}11]$ directions converts to a single state (Fig. 1c and d) which only contains domain walls along $[01\bar{1}]$ direction with increasing the film thickness. Another feature is that the density of domains increases dramatically when decreasing the thickness of PTO films. It was reported that there are inclined and normal {101} domain walls in (111)- oriented ferroelectric tetragonal films along <110> and <112> directions, respectively [27]. So it is possible that our PTO films are tetragonal with domain walls along $[01\bar{1}]$ and $[\bar{2}11]$ directions. Based on this hypothesis and misfit strain analysis in Table 1, it can be deduced that domain walls of d_2^+/d_3^+ or d_2/d_3 domains are along $[01\bar{1}]$, and domain walls of d_2^-/d_3^+ or d_2/d_3 domains are along $[\bar{2}11]$. The lattice characteristics of d_2^+/d_3^+ domains are the same as d_2/d_3 domains except for out-of-plane polarization component, so only d_2^+/d_3^+ domains are taken in consideration for simplicity, and the same for d_2^-/d_3^+ domains.

It is noteworthy that the domain walls of d_2^+/d_3^+ is invisible when observing from $[01\bar{1}]$ directly, as shown in Figure S2a. The atomic structure schematics of d_2^+ and d_3^+ domains are shown in Figure S2b. From Figure S2b, we can see that both the polarization component direction and the c-axis component in $(01\bar{1})$ plane are the same for d_2^+/d_3^+ domains, so the domain walls are invisible when observed from $[01\bar{1}]$ direction. But when we tilt the sample to $[12\bar{3}]$ or $[\bar{1}3\bar{2}]$ zone axis, the inclined domain walls can be clearly seen as shown in Figure S2c, d. The polarization vector and c-axis component of d_2^+ and d_3^+ become different by tilting the sample about 19° from $[01\bar{1}]$ to $[12\bar{3}]$ or $[\bar{1}3\bar{2}]$, then the stripe domains with inclined domain boundaries will come out. From S2c and S2d, the angles between domain walls and interface are about 37° which is close to the angle between (011) and (111). Thus it can be deduced that the
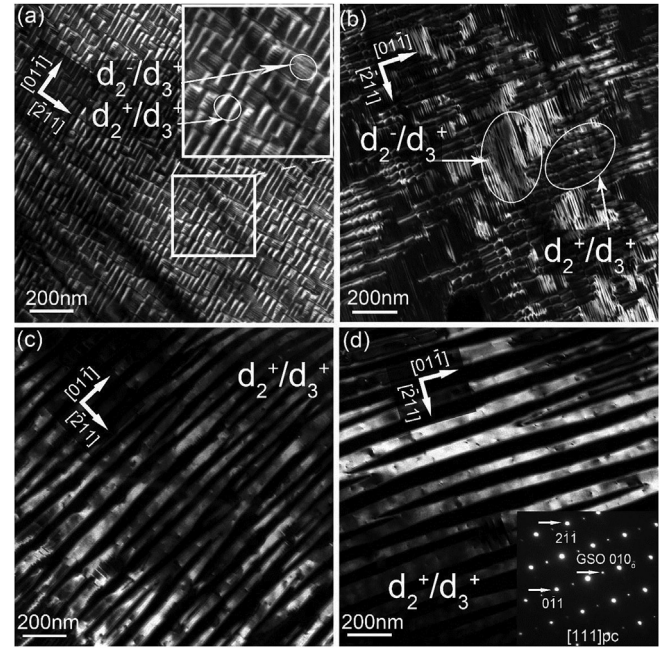

Fig. 1. Plane view TEM images of PTO films on GSO substrates: (a) 8 nm, (b) 20 nm, (c) 50 nm, (d) 90 nm. The inset in (a) shows the enlargement of white rectangle in (a); the insert SAED pattern in (d) denotes the domain walls are along $[01\bar{1}]$.

domain wall of d_2^+/d_3^+ domains may be (011). The angles of $[01\bar{1}]$/$[12\bar{3}]$, and $[01\bar{1}]$/$[\bar{1}3\bar{2}]$ are both about 19° as calculated and depicted in figure S2e. Detailed analysis of these is in the following context by selected area electron diffraction (SAED) and high resolution (HR) high angle annular dark field (HAADF) scanning transmission electronic microscopy (STEM).

In order to confirm our deduction and make a further study of the domain structures, cross-view TEM samples with each thickness were prepared from both $[01\bar{1}]$ and $[11\bar{2}]$ directions. Fig. 2 shows the cross-sectional dark field TEM images of different thick PTO films from $[12\bar{3}]$ and $[\bar{2}11]$ zone axes. It can be seen that both the interfaces of films/substrates and the surfaces of films are flat in all films. There are two different domain morphologies. The one is with the domain walls inclined to the interface, and the other, normal to the interface. Now, the two kinds of domain walls can be determined as (011) and $(01\bar{1})$ for d_2^+/d_3^+ domains and d_2^-/d_3^+ domains, respectively. Consistent with the plan-view TEM observation, d_2^+/d_3^+ domains with inclined domain walls are periodically distributing in all of the films, while the d_2^-/d_3^+ domains with domain walls along $[\bar{2}11]$ direction exist only in thinner films. In the thicker PTO films (50 nm and 90 nm), some vertical contrasts, which are different from d_2^-/d_3^+ domains, mainly come from misfit dislocations for the relative large misfit strain along $<01\bar{1}>$ direction. The domain structures of ferroelectric films are usually influenced by elastic and electrostatic boundary conditions [15,16,18,20,34]. Only the d_2 and d_3 domains are formed in all of the films is a result of elastic energy minimization as analyzed in

Table 1
Lattice parameters and misfit strains of GSO and $d_1/d_2/d_3$ domains.

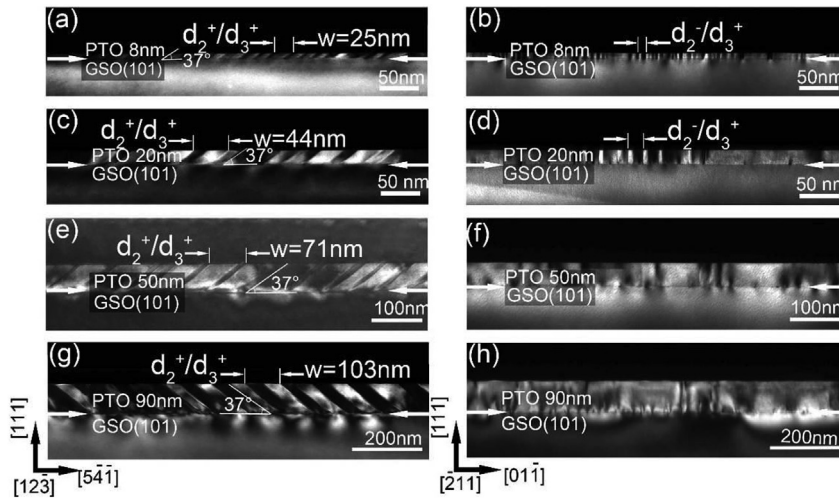|	$d_{(01\bar{1})}$	$d_{(2\bar{1}\bar{1})}$	$d_{(1\bar{1}0)}$	$d_{(11\bar{2})}$	$d_{(\bar{1}01)}$	$d_{(1\bar{2}1)}$
GSO	2.879	1.607	2.806	1.648	2.806	1.648
d_1	2.757 (4.2%)	1.655 (−3%)	2.838 (−1.1%)	1.607 (2.5%)	2.838 (−1.1%)	1.607 (2.5%)
d_2	2.838 (1.4%)	1.607 (0%)	2.757 (1.7%)	1.655 (−0.4%)	2.838 (−1.1%)	1.607 (2.5%)
d_3	2.838 (1.4%)	1.607 (0%)	2.838 (−1.1%)	1.607 (2.5%)	2.757 (1.7%)	1.655 (−0.4%)

Fig. 2. Cross-sectional TEM images of PTO films with different thicknesses grown on GSO (101)o substrates. (a)(b) 8 nm; (c)(d) 20 nm; (e)(f) 50 nm; (g)(h) 90 nm. W represents the width of d_2^+/d_3^+ domain structure. (a)(c)(e)(g): taken from [12$\overline{3}$] zone axis, and (b) (d) (f) (h): taken from [$\overline{2}$11] zone axis.

Table 1. When decreasing the thickness of PTO, d_2^-/d_3^+ domains with opposite out-of-plane polarization components are formed in 8 nm and 20 nm PTO films. The formation of these kinds of domains may be a result of either the accumulation of surface charges [35,36] or the increase of depolarization field [18,37,38]. The depolarization field is dependent on the thickness of the film and dielectric properties of "dead layers", which is the layer separating the ferroelectric film from the real electrode [39]. Since our PTO films were deposited on insulated substrate and no real electrodes were used, the depolarization field of the four PTO films reaches its maximum. It was reported that the domain structure can be rebuilt by the surface charges through flexochemical coupling in thin ferroelectric films [36]. Particularly, with the decrease of film thickness, the effect of surface charging on domain formation is becoming more and more obvious. Thus, the formation of d_2^-/d_3^+ domains in thinner PTO films cannot be simply interpreted by the increment in depolarization field. In this way, the formation of d_2^-/d_3^+ domains in the thinner PTO films may be mainly ascribed to the surface screening charges.

In order to further verify and reveal the structure information of d_2^+/d_3^+ and d_2^-/d_3^+ domains, SAED and HR HAADF STEM are performed. The SAED patterns obtained from the areas including both d_2^+/d_3^+ domains and substrates in 90 nm PTO films are displayed in Fig. 3a and b, respectively, and indexed as [01$\overline{1}$] and [12$\overline{3}$] zone axes. The spot splitting for high-index spots can be discernible as denoted by white circles. In Fig. 3a, the diffraction spots only show splitting along the out-of-plane direction, indicating different out-of-plane d-spacings between substrates and films. It can be deduced that the inner diffraction spots are from PTO due to the large d-spacing of (111) lattice plane. It is also noted that the diffraction spots of d_2^+ domains and d_3^+ domains cannot be distinguished due to the same lattice parameters when observed along [01$\overline{1}$] zone axis as depicted in Figure S2b. Luckily, the diffraction spots of d_2^+ and d_3^+ domains can be distinguished when tilting the sample about 19° around [111] direction from [01$\overline{1}$] to [12$\overline{3}$] zone axis as shown in Fig. 3b. From Fig. 3b, we can see that while the diffraction spots along out-of-plane direction [111] keep unchanged, some spots along other directions are split implying the coexistence of multiple domains. For the d_2^-/d_3^+ domains, Fig. 3c is given which is a SAED pattern of 20 nm thick PTO films taken from the area including both the films and the substrates along [$\overline{2}$11] direction. It is noted that spot splitting along out-of-plane direction

[111] are evident. To further determine the phase structure and understand the details of Fig. 3a, b and 3c, the enlargement patterns corresponding to the spots outlined by boxes and numbered 1–4 in each figure are shown in Fig. 3d, e, 3f and 3g, respectively. In Fig. 3d, the enlargement of 222 spot reveals the spot splitting, indicating the difference in out of plane lattice parameters of films and substrates. In Fig. 3e, the 222 spot keeps unchanged. However, the spot splitting of 2$\overline{1}$0 is clearly discernible and shown in Fig. 3f. Three spots can be identified and indexed as 2$\overline{1}$0 of d_2^+, d_3^+ and GSO, respectively, according to the lattice parameters of PTO and GSO [31,32], which verifies the coexistence of both d_2^+ and d_3^+ domains. The relative angles of (2$\overline{1}$0) plane between d_2^+, d_3^+ domains and substrates extracted from diffraction deflection are 3.6° and 1.8° which are close to bulk values (3.3° and 1.3°). The enlargement of 120 reflection in Fig. 3b is displayed in Fig. 3g, which was chosen instead of 111 reflection because the spot splitting can be more clearly identified. The strongest spot in the center of Fig. 3g is indexed as 120 of GSO, while the two weak spots on the both sides of GSO 120 spot are indexed as 120 of d_2^+ and d_3^+ domains, respectively. Thus, it can be further confirmed that the inclined domain walls (011) formed by d_2^+/d_3^+ domains exist in all of the films, while the normal domain walls (01$\overline{1}$) formed by d_2^-/d_3^+ domains only exist in thinner films (8 nm and 20 nm).

Further study demonstrates that the width of the d_2^+/d_3^+ domains shows a positive correlation with the film thickness. To clarify the explicit correlation, the domain width and film thickness are summarized and shown in Fig. 4. The scattering points in Fig. 4 were obtained from different areas of cross-view TEM images. The data was then fitted in origin software via two fitting curves: $y = a + bx$ for linear fit and $y = a * x^b$ for curve fit. The results for $y = a * x^b$ are a = 9.34 and b = 0.53 with standard errors of 1.31 and 0.03, respectively; while for $y = a + bx$, the results are a = 26.14, and b = 0.901 with standard errors of 2.89 and 0.06. Since the standard errors of the linear fit are about twice of the curve fit, the curve fit is more appropriate to describe the relationship between domain width and film thickness as indicated by the black solid line shown in Fig. 4, which is satisfied with W $\propto$ d$^{1/2}$. Such a relationship between the domain period and film thickness was initially proposed by Kittel for ferromagnetic systems [40], and then was extended to ferroelectric systems by Mitsui and Furuichi (KMF's law) [41,42]. It was also reported that the domain wall broadening may occur near electrically-open surfaces, then the relationship between domain
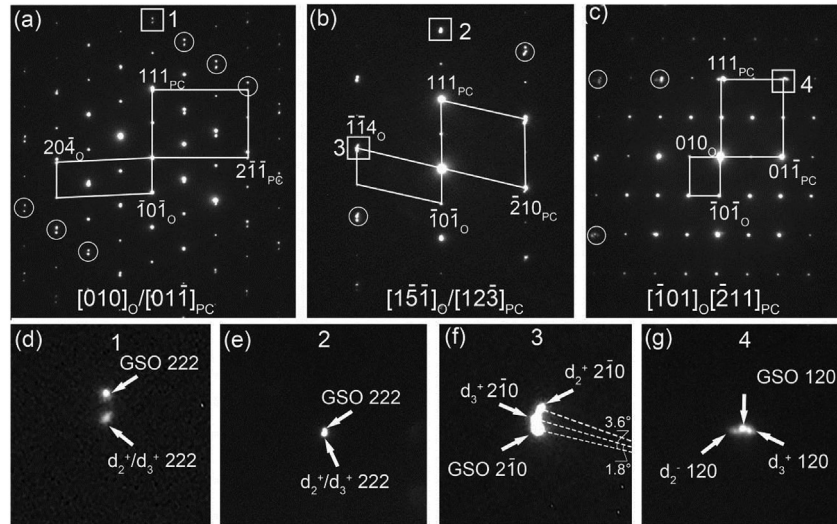
Fig. 3. Selected area electron diffraction (SAED) patterns of PTO films on *GSO* substrates. (a) (b) SAED patterns for 90 nm thick PTO films taken from the areas including the substrates and d_2^+/d_3^+ domains; (c) SAED pattern taken from the area including the substrate and d_2^-/d_3^+ domains for 20 nm thick PTO films; (d—f) are the enlargements of the rectangles marked in (a—c).
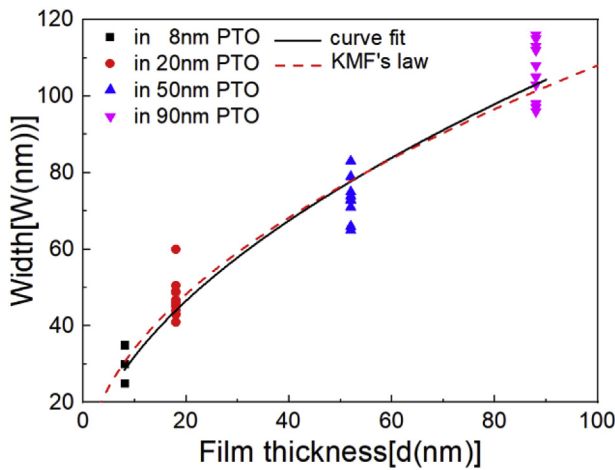

Fig. 4. The observed domain width (W) of periodic d_2^+/d_3^+ domains as a function of film thickness (d) for PTO thin films grown on GSO substrates. The curve fit is close to KMF's law (W ∝ d^1/2).

period and film thickness will deviate from KMF's law [35]. The PTO films in the present study have all common 90° domain walls without any domain wall broadening. Thus the "KMF's law" can be used to describe the relationship between domain width and film thickness in the PTO films.

HR-HAADF-STEM imaging was carried out to clarify the atomic structures of d_2^-/d_3^+ and d_2^+/d_3^+ domains from [$\bar{2}$11], [111] and [12$\bar{3}$] directions, respectively. The atomic structure schematics of d_3^+ and d_2^- domains observed from [$\bar{2}$11] direction are shown in Fig. 5a and b, in which only Pb columns are displayed. The Ti and O columns are removed and the c-axis are enlarged 20% in all schematics for explicitation. It can be derived that the lattice characteristics are strongly correlated with the c-axis orientation. For d_3^+ domains in Fig. 5a, whose c-axis are along [001], the (111) planes marked by a green line rotate clockwise relative to the horizontal plane represented by the dashed line, while in Fig. 5b, the (111) planes of d_2^- domains indicated by a red line rotate anticlockwise, *i.e.* the lattice of d_3^+ domains rotates clockwise relative to d_2^- domains. In order to directly reveal the lattice characteristics, a cross-sectional atomic

resolved HAADF STEM image of the 20 nm thick PTO/GSO thin films from [$\bar{2}$11] direction is shown in Fig. 5c, where the alternately distributed d_2^- and d_3^+ domains are evident and separated by light blue domain walls. The c-axis orientations denoted by red and green arrows are obtained from the rotation characteristics of (111) plane as described in Fig. 5a and b. Similar to Fig. 5a and b, the lattice of d_3^+ domains rotates clockwise respect to d_2^- domains from [111] zone axis as depicted in Fig. 5d and e. A HR-HAADF-STEM image of plane-view samples in 20 nm PTO films from [111] direction showing the alternately distributed d_2^- and d_3^+ domains are displayed in Fig. 5f, where the light blue dash lines represent the (01$\bar{1}$) domain walls, and the arrows denote the c-axis orientations. The 2.4° misorientation angles of d_2^- and d_3^+ domains can be revealed as indicated by the red and green lines in Fig. 5f. The inclined domain walls (011) of d_2^+ and d_3^+ domains are along [01$\bar{1}$] direction, but the domain walls can only be observed from [12$\bar{3}$] or [$\bar{1}$3$\bar{2}$] directions as analyzed in Figure S2. Detailed analysis is shown in Fig. 5g—i. Fig. 5g and h shows the atomic structure schematics observed from [01$\bar{1}$] and [12$\bar{3}$] directions for d_3^+ and d_2^+ domains, respectively. When observed from [01$\bar{1}$] direction, the d-spacing and the angles between lattice-planes are the same for both d_3^+ and d_2^+ domains. While tilting the sample to [12$\bar{3}$] direction, for bulk PTO, the in-plane ($\bar{5}$41) d-spacings for d_3^+ and d_2^+ domains are 0.60 Å and 0.61 Å, respectively, and the angles between (111) and (2$\bar{1}$0) are 74.7° and 72.7°, respectively [31]. It is noted that the out-of-plane d-spacings are equal for both cases. To testify this deduction, an atomic resolved HAADF STEM image of 90 nm PTO films is shown in Fig. 5i, in which the arrows denote the c-axis orientation. It is observed that the sharp (011) domain wall turns to a domain wall area with the width of around 1 nm after tilting the sample from [01$\bar{1}$] to [12$\bar{3}$] zone axis as denoted by the shade light blue area. The angles between (111) and (2$\bar{1}$0) are denoted by the blue and green parallelograms on both sides of the domain wall area, which is close to bulk value. It is also noted that the misorientation angle 2.2° of d_2^-/d_3^+ domains can be revealed as indicated by the blue and green lines in Fig. 5i. The inset in Fig. 5i is a schematic showing the lattice rotation with an angle of approximately 2.2° on two sides of d_2^-/d_3^+ domain wall. The fast Fourier transform (FFT) patterns for Fig. 5c, f, and 5i are shown in Figure S3, where the high-index FFT spot splittings can be easily detected to verify the
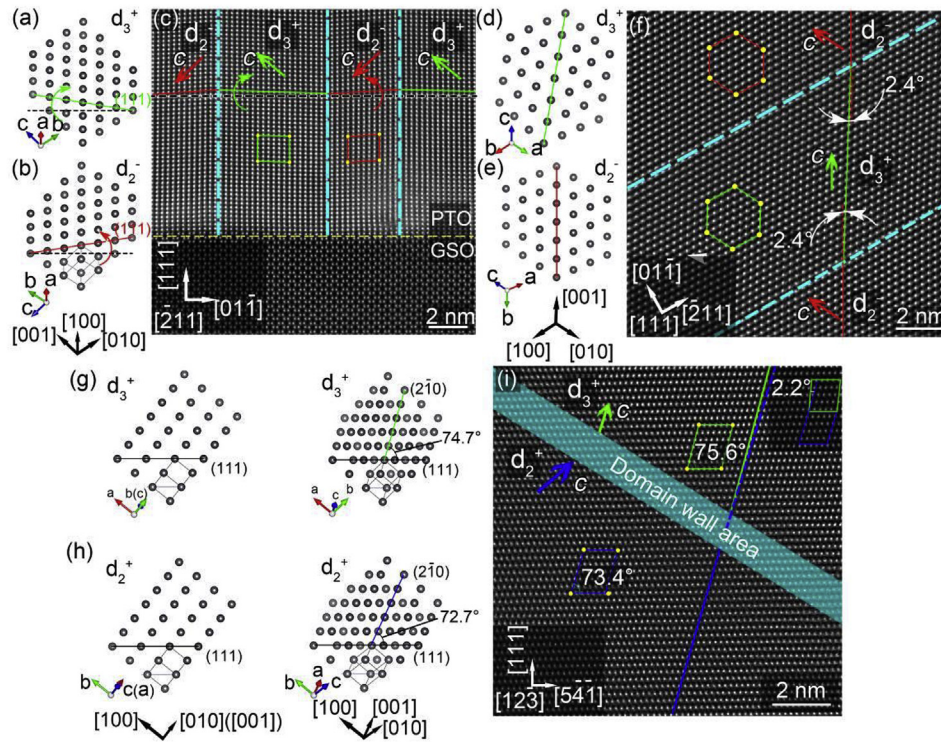
Fig. 5. Atomic structure schematics and High-resolution HAADF-STEM image of the two kinds of domain walls. (a) (b)Atomic structure schematics of d_3^+ and d_2^- domains observed from [$\bar{2}$11] direction; (c) High-resolution HAADF-STEM image taken along [$\bar{2}$11] showing the intersection of d_2^-/d_3^+ domains in 20 nm thick PTO films from cross-sectional observations; (d) (e) Atomic structure schematics of d_3^+ and d_2^- domains observed from [111]; (f) High-resolution HAADF-STEM image showing the intersection of d_2^-/d_3^+ domains from [111] in plane-view observations; (g)Atomic structure schematics of d_3^+ observed from [01$\bar{1}$] (left) and [12$\bar{3}$] (right) directions, respectively; (h)Atomic structure schematic of d_2^+ domains observed from [01$\bar{1}$] (left) and [12$\bar{3}$](right), respectively; (i) High-resolution HAADF-STEM image showing the intersection of d_2^+/d_3^+ domains in 90 nm thick PTO films from [12$\bar{3}$] in cross-view samples. Arrows in (c) (f) (i) represent the magnitude and direction of c-axis's projection. The c-axis in all schematics are enlarged 20% for explicitation.

existence of ferroelectric domains, which are similar to SAED patterns displayed in Fig. 3.

For further revealing the details of the d_2^+/d_3^+ and d_2^-/d_3^+ domains, low magnification HAADF-STEM imaging of the PTO films and corresponding geometric phase analysis (GPA) [43–45] including lattice rotation and lattice strains were conducted and shown in Fig. 6 and Figure S4. Fig. 6a shows the HAADF-STEM image of alternately distributed d_2^- and d_3^+ domains, where the light blue dash lines represent the domain walls, and the green and red arrows denote the c-axis orientations. The in-plane lattice rotation (R_x) mapping of Fig. 6a is shown in Fig. 6b, and the corresponding line profiles performed from left to right along the routes labeled rotation profiles 1 and 2 are shown in Fig. 6c. If the R_x of substrate is set to zero, the R_x of d_2^- would be positive according to the analysis of HR-HAADF-STEM image in Fig. 5, while the R_x of d_3^+ would be negative. In this way, we can confirm the alternate distribution of d_2^-/d_3^+ domains. The in-plane and out-of-plane strain mappings are shown in Figure S4a and S4b. It can be seen that both in-plane and out-of-plane lattice strains are uniformly distributed for the d_2^-/d_3^+ domains due to the same components of c-axis along in-plane and out-of-plane directions. Fig. 6d shows the plane-view HAADF-STEM image of d_2^-/d_3^+ domains in 20 nm thick PTO film. The corresponding lattice rotation, in-plane and out-of-plane lattice strain mappings are shown in Fig. 6e, S4d and S4e, respectively. Based on the previous analysis in Fig. 5f, the lattice of d_2^- domains rotates about 3.5° anticlockwise respect to d_3^+ domains along [111] direction. That is to say, if the lattice rotation (ω) of d_3^+ is set to zero, the ω of d_2^- domains would be 3.5° as depicted in Fig. 6f. The in-plane and out-of-plane lattice strain variations are shown in Figure S4d and S4e. The d_2^- domains are in red and the d_3^+ domains are in green

in Figure S4d, while their colors are opposite in Figure S4e as a result of different c-axis orientations which are represented by red and green arrows in Fig. 6d. The HAADF-STEM image of d_2^+/d_3^+ domains including substrates and the corresponding out-of-plane lattice rotation (R_y) mapping are shown in 6 g and 6 h. From the lattice rotation map, comparing with the substrate, the d_2^+ domain is in green, while d_3^+ domain is in red, indicating the out-of-plane lattice of d_2^+ domain rotates clockwise respect to the substrate, while the out-of-plane lattice of d_3^+ domain rotates anticlockwise respect to d_2^+ domain. To make it clearly, a line profile along the route labeled rotation profile 4 in Fig. 6h from bottom to top is shown in Fig. 6i, which reveals the out-of-plane lattice rotations are approximate −3° and −1.2° for d_2^+ and d_3^+ domains, respectively. The corresponding in-plane and out-of-plane lattice strains are shown in Figure S4g and S4h, respectively. It is pointed out that the in-plane component of c-axis in d_2^+ domains is larger than that in d_3^+ domains, and the out-of-plane component keeps unchanged for both domains. Accordingly, the in-plane lattice strain in d_2^+ is larger than that in d_3^+, while the out-of-lattice strain is identical for the two kinds of domains as displayed in Figure S4g and S4h.

Detailed (S)TEM studies of (111) oriented PTO films epitaxially grown on GSO shown above reveal that there are two kinds of domain walls: "inclined" and "normal" lying on (011) and (01$\bar{1}$) planes, respectively. The schematics of these domain walls are shown in Fig. 7a and (b). In Fig. 7a, d_2^+ (blue arrows) and d_3^+ (green arrows) represent the domains whose ferroelectric polarizations are along [010] and [001], respectively. The right side of Fig. 7a illustrates the in-plane (upper) and out-of-plane (lower) polarization component distributions of d_2^+ and d_3^+ domains. The out-of-plane polarization component is uniform while the angle between in-
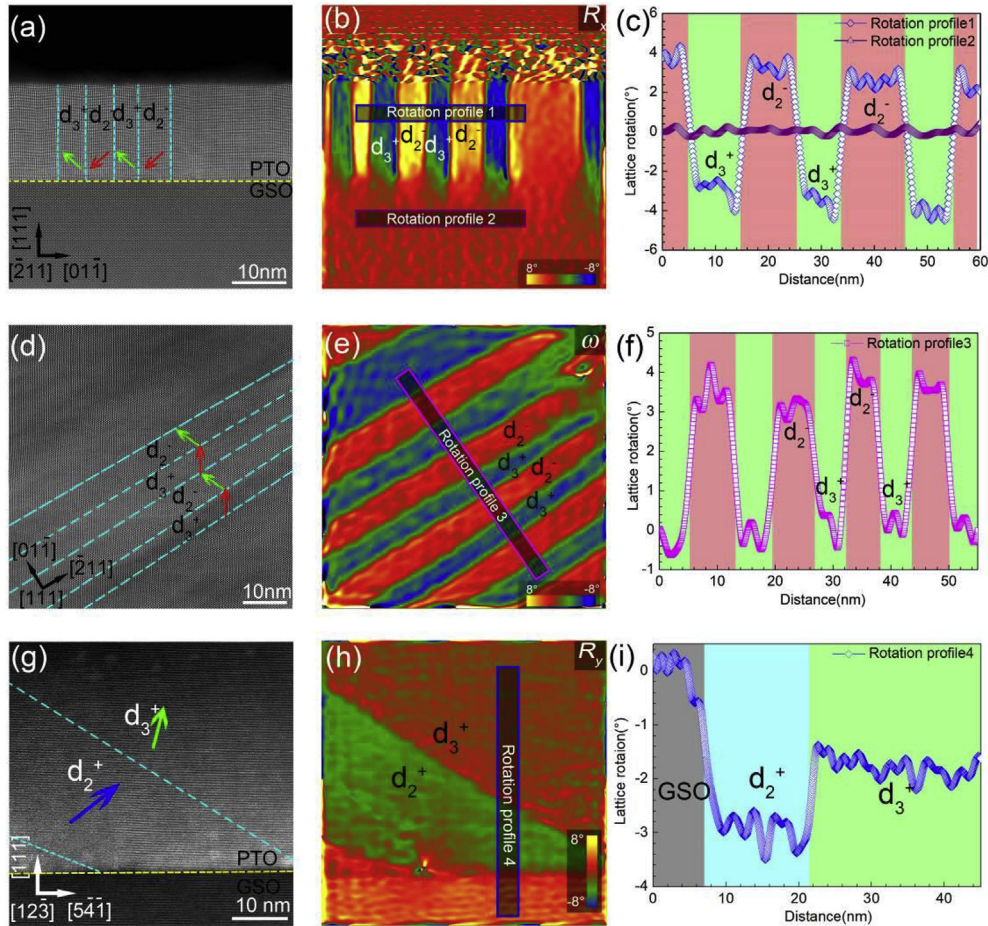
Fig. 6. GPA analysis of $d_{\bar{2}}/d_{\bar{3}}^+$ and $d_{\bar{2}}^+/d_{\bar{3}}^+$ domains. (a) Cross-sectional HAADF-STEM image of the 20 nm thick films containing $d_{\bar{2}}/d_{\bar{3}}^+$ domains taken from [$\bar{2}11$] and (b) corresponding lattice-x rotation (R_x) map; (c)Line profiles labeled in (b); (d) Plane-view HAADF-STEM image of the 20 nm thick film containing $d_{\bar{2}}/d_{\bar{3}}^+$ domains taken from [111] direction and (e) corresponding lattice rotation (ω) map; (f)Line profile labeled in (e); (g) Cross-sectional HAADF-STEM image of the 90 nm films containing $d_{\bar{2}}^+/d_{\bar{3}}^+$ domains taken from [$12\bar{3}$] direction and (h)corresponding Lattice-y rotation (R_y) map; (i)Line profile labeled in (h). Arrows in (a) (d) (g) represent the magnitude and direction of c-axis's projection.
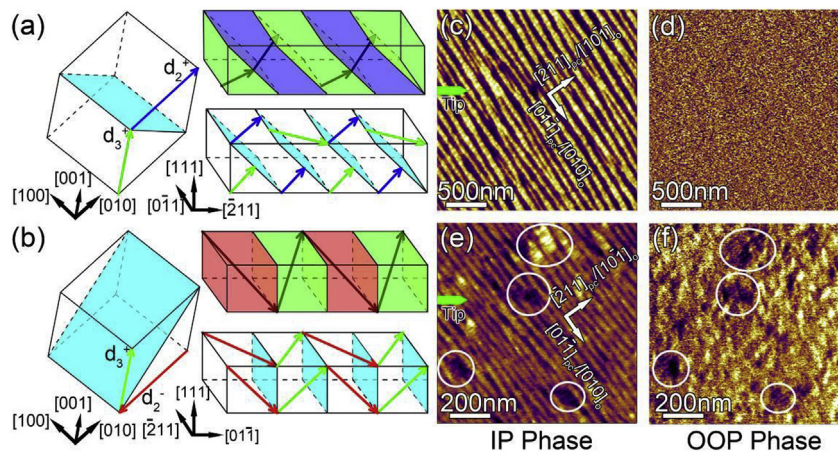

Fig. 7. Schematics and PFM phase images of the two kinds of domain walls. (a)(b) Schematics of inclined and normal domain walls; Arrows indicate the orientation of c-axis; (c)(d) IP Phase and OOP Phase images of 90 nm PTO films; (e)(f) IP Phase and OOP Phase images of 20 nm PTO films; White circles in (e) and (f) denote domain walls perpendicular to stripe domain walls.

plane polarization components is about 120°. Oppositely, as shown in Fig. 7b, the in-plane and out-of-plane polarization are both different for $d_{\bar{2}}$ (red arrows) and $d_{\bar{3}}^+$ (green arrows) domains. To support the analysis, PFM measurements were carried out. PFM

images (Fig. 7c−f) confirm the differences between $d_{\bar{2}}^+/d_{\bar{3}}^+$ and $d_{\bar{2}}/d_{\bar{3}}^+$ domains of (111)-oriented PTO films. For the 90 nm PTO films, the in-plane (IP) phase image (Fig. 7c), taken with the cantilever along [$\bar{1}10$], shows stripe contrast throughout the whole film.

However, the out-of-plane (OOP) phase image (Fig. 7d) shows uniform contrast, indicating identical out-of-plane polarization components in the two kinds of domains. In the 20 nm thick PTO films, besides the area with stripe IP phase (Fig. 7e) and uniform OOP phase (Fig. 7f), taken with the cantilever along [$\bar{1}$10], both IP and OOP phase images show stripe contrasts in circled areas. This indicates difference in both in-plane and out-of-plane polarization components which match the characteristics of d_2^-/d_3^+ domains as depicted in Fig. 7b. The local hysteresis loops for the four PTO films were also measured by PFM, which are shown in figure S5. It can be seen that local PFM spectroscopic measurements for the films all exhibit bipolar piezoelectric hysteresis loops. The local coercive field of each film can be obtained according to the film thickness and local positive and negative coercive voltages marked by red arrows in figure S5a-5d. The results are 862 MV/m, 270 MV/m, 26.5 MV/m and 13 MV/m for 8 nm, 20 nm, 50 nm and 90 nm, respectively, which shows a negative correlation with film thickness which is consistent with experiment observations reported previously [24,46].

4. Conclusion

In summary, we have demonstrated an effective way to control the domain structure in (111)- oriented PTO films. By using the anisotropic strain imposed by the GSO $(101)_O$ substrate, three tetragonal distortions can be reduced to two distortions (d_2 and d_3). In the thick films, one-dimensional, periodic nanoscale arrays of both d_2^-/d_3^+ and d_2^-/d_3^- domains with inclined domain walls (011) along [01$\bar{1}$] are formed in PTO films. With decreasing the film thickness, high density d_2^-/d_3^+ and d_2^-/d_3^- domains with normal domain walls (01$\bar{1}$) along [$\bar{2}$11], which are perpendicular to the former domain wall direction, are further formed due to the surface screening charge accumulations. These results disclose the strain effect on domain configurations in (111)- oriented PTO films and uncover the domain evolution with film thickness. The controlled domain structure provides us help to further explore the functional properties of domains and domain walls in (111)-oriented PTO films.

Acknowledgement

Appendix A. Supplementary data

Supplementary data to this article can be found online at https://doi.org/10.1016/j.actamat.2019.01.005.

References

[1] J. Hoffman, X. Pan, J.W. Reiner, F.J. Walker, J.P. Han, C.H. Ahn, T.P. Ma, Ferroelectric field effect transistors for memory applications, Adv. Mater. 22 (26–27) (2010) 2957–2961.

[2] J. Scott, Applications of modern ferroelectrics, Science 315 (5814) (2007) 954–959.

[3] P. Muralt, Ferroelectric thin films for micro-sensors and actuators: a review, J. Micromech. Microeng. 10 (2) (2000) 136.

[4] C.-B. Eom, S. Trolier-McKinstry, Thin-film piezoelectric MEMS, MRS Bull. 37 (11) (2012) 1007–1017.

[5] E.Y. Tsymbal, H. Kohlstedt, Tunneling across a ferroelectric, Science 313 (5784) (2006) 181–183.

[6] Y.L. Li, S.Y. Hu, Z.K. Liu, L.Q. Chen, Phase-field model of domain structures in ferroelectric thin films, Appl. Phys. Lett. 78 (24) (2001) 3878–3880.

[7] Y. Li, S. Hu, Z. Liu, L. Chen, Effect of substrate constraint on the stability and evolution of ferroelectric domain structures in thin films, Acta Mater. 50 (2) (2002) 395–411.

[8] O. Nesterov, S. Matzen, C. Magen, A.H.G. Vlooswijk, G. Catalan, B. Noheda, Thickness scaling of ferroelastic domains in $PbTiO_3$ films on $DyScO_3$, Appl. Phys. Lett. 103 (14) (2013) 142901.

[9] S. Li, Y.L. Zhu, Y.L. Tang, Y. Liu, S.R. Zhang, Y.J. Wang, X.L. Ma, Thickness-dependent a_1/a_2 domain evolution in ferroelectric $PbTiO_3$ films, Acta Mater. 131 (2017) 123–130.

[10] Y. Tang, Y. Zhu, X. Ma, A.Y. Borisevich, A.N. Morozovska, E.A. Eliseev, W. Wang, Y. Wang, Y. Xu, Z. Zhang, Observation of a periodic array of flux-closure quadrants in strained ferroelectric PbTiO3 films, Science (2015) 1259869.

[11] Y. Liu, Y.J. Wang, Y.L. Zhu, C.H. Lei, Y.L. Tang, S. Li, S.R. Zhang, J. Li, X.L. Ma, Large scale two-dimensional flux-closure domain arrays in oxide multilayers and their controlled growth, Nano Lett. 17 (12) (2017) 7258–7266.

[12] A.K. Yadav, C.T. Nelson, S.L. Hsu, Z. Hong, J.D. Clarkson, C.M. Schleputz, A.R. Damodaran, P. Shafer, E. Arenholz, L.R. Dedon, D. Chen, A. Vishwanath, A.M. Minor, L.Q. Chen, J.F. Scott, L.W. Martin, R. Ramesh, Observation of polar vortices in oxide superlattices, Nature 530 (7589) (2016) 198–201.

[13] A.R. Damodaran, J.D. Clarkson, Z. Hong, H. Liu, A.K. Yadav, C.T. Nelson, S.L. Hsu, M.R. McCarter, K.D. Park, V. Kravtsov, A. Farhan, Y. Dong, Z. Cai, H. Zhou, P. Aguado-Puente, P. Garcia-Fernandez, J. Iniguez, J. Junquera, A. Scholl, M.B. Raschke, L.Q. Chen, D.D. Fong, R. Ramesh, L.W. Martin, Phase coexistence and electric-field control of toroidal order in oxide superlattices, Nat. Mater. 16 (10) (2017) 1003–1009.

[14] Q. Zhang, L. Xie, G. Liu, S. Prokhorenko, Y. Nahas, X. Pan, L. Bellaiche, A. Gruverman, N. Valanoor, Nanoscale bubble domains and topological transitions in ultrathin ferroelectric films, Adv. Mater. 29 (46) (2017).

[15] D.G. Schlom, L.-Q. Chen, C.-B. Eom, K.M. Rabe, S.K. Streiffer, J.-M. Triscone, Strain tuning of ferroelectric thin films, Annu. Rev. Mater. Res. 37 (1) (2007) 589–626.

[16] A.R. Damodaran, J.C. Agar, S. Pandya, Z. Chen, L. Dedon, R. Xu, B. Apgar, S. Saremi, L.W. Martin, New modalities of strain-control of ferroelectric thin films, J. Phys. Condens. Matter 28 (26) (2016) 263001.

[17] A.R. Damodaran, S. Pandya, J.C. Agar, Y. Cao, R.K. Vasudevan, R. Xu, S. Saremi, Q. Li, J. Kim, M.R. McCarter, L.R. Dedon, T. Angsten, N. Balke, S. Jesse, M. Asta, S.V. Kalinin, L.W. Martin, Three-state ferroelastic switching and large electromechanical responses in $PbTiO_3$ thin films, Adv. Mater. 29 (37) (2017).

[18] C.T. Nelson, B. Winchester, Y. Zhang, S.J. Kim, A. Melville, C. Adamo, C.M. Folkman, S.H. Baek, C.B. Eom, D.G. Schlom, L.Q. Chen, X. Pan, Spontaneous vortex nanodomain arrays at ferroelectric heterointerfaces, Nano Lett. 11 (2) (2011) 828–834.

[19] C. Lichtensteiger, S. Fernandez-Pena, C. Weymann, P. Zubko, J.M. Triscone, Tuning of the depolarization field and nanodomain structure in ferroelectric thin films, Nano Lett. 14 (8) (2014) 4205–4211.

[20] G. Liu, J. Chen, C. Lichtensteiger, J.-M. Triscone, P. Aguado-Puente, J. Junquera, N. Valanoor, Positive effect of an internal depolarization field in ultrathin epitaxial ferroelectric films, Advanced Electronic Materials 2 (1) (2016) 1500288.

[21] L. Feigl, P. Yudin, I. Stolichnov, T. Sluka, K. Shapovalov, M. Mtebwa, C.S. Sandu, X.K. Wei, A.K. Tagantsev, N. Setter, Controlled stripes of ultrafine ferroelectric domains, Nat. Commun. 5 (2014) 4677.

[22] R. Xu, S. Liu, I. Grinberg, J. Karthik, A.R. Damodaran, A.M. Rappe, L.W. Martin, Ferroelectric polarization reversal via successive ferroelastic transitions, Nat. Mater. 14 (1) (2015) 79–86.

[23] R. Xu, J. Karthik, A.R. Damodaran, L.W. Martin, Stationary domain wall contribution to enhanced ferroelectric susceptibility, Nat. Commun. 5 (2014) 3120.

[24] R. Xu, R. Gao, S.E. Reyes-Lillo, S. Saremi, Y. Dong, H. Lu, Z. Chen, X. Lu, Y. Qi, S.L. Hsu, A.R. Damodaran, H. Zhou, J.B. Neaton, L.W. Martin, Reducing coercive-field scaling in ferroelectric thin films via orientation control, ACS Nano 12 (5) (2018) 4736–4743.

[25] R. Xu, J. Zhang, Z. Chen, L.W. Martin, Orientation-dependent structural phase diagrams and dielectric properties of $PbZr_{1-x}Ti_xO_3$ polydomain thin films, Phys. Rev. B 91 (14) (2015).

[26] T. Yamada, J. Yasumoto, D. Ito, O. Sakata, Y. Imai, T. Kiguchi, T. Shiraishi, T. Shimizu, H. Funakubo, M. Yoshino, T. Nagasaki, Negligible substrate clamping effect on piezoelectric response in (111)-epitaxial tetragonal Pb(Zr, Ti)O_3 films, J. Appl. Phys. 118 (7) (2015), 072012.

[27] A. Romanov, A. Vojta, W. Pompe, M. Lefevre, J. Speck, Domain patterns in (111) oriented tetragonal ferroelectric films, Phys. Status Solidi 172 (1) (1999) 225–253.

[28] R. Oja, K. Johnston, J. Frantti, R.M. Nieminen, Computational study of (111) epitaxially strained ferroelectric perovskites $BaTiO_3$ and $PbTiO_3$, Phys. Rev. B 78 (9) (2008).

[29] T. Angsten, L.W. Martin, M. Asta, Orientation-dependent properties of epitaxially strained perovskite oxide thin films: insights from first-principles calculations, Phys. Rev. B 95 (17) (2017).

[30] C. Ophus, J. Ciston, C.T. Nelson, Correcting nonlinear drift distortion of scanning probe and scanning transmission electron microscopies from image pairs with orthogonal scan directions, Ultramicroscopy 162 (2016) 1–9.

[31] G. Shirane, S. Hoshino, On the phase transition in lead titanate, J. Phys. Soc. Jpn. 6 (4) (1951) 265–270.

[32] S. Amanyan, Electrical and optical properties of $Lu_XGd_{1-X}SCO_3$ crystals activated with Nd^{3+}, Inorg. Mater. 20 (7) (1984) 1029.

[33] V. Nagarajan, I.G. Jenkins, S.P. Alpay, H. Li, S. Aggarwal, L. Salamanca-Riba, A.L. Roytburd, R. Ramesh, Thickness dependence of structural and electrical properties in epitaxial lead zirconate titanate films, J. Appl. Phys. 86 (1) (1999) 595–602.

[34] Y.-H. Chu, Q. He, C.-H. Yang, P. Yu, L.W. Martin, P. Shafer, R. Ramesh, Nanoscale control of domain architectures in $BiFeO_3$ thin films, Nano Lett. 9 (4) (2009) 1726–1730.

[35] I.S. Vorotiahin, E.A. Eliseev, Q. Li, S.V. Kalinin, Y.A. Genenko, A.N. Morozovska, Tuning the polar states of ferroelectric films via surface charges and flexoelectricity, Acta Mater. 137 (2017) 85–92.

[36] E.A. Eliseev, I.S. Vorotiahin, Y.M. Fomichov, M.D. Glinchuk, S.V. Kalinin, Y.A. Genenko, A.N. Morozovska, Defect-driven flexochemical coupling in thin ferroelectric films, Phys. Rev. B 97 (2) (2018).

[37] S.K. Streiffer, J.A. Eastman, D.D. Fong, C. Thompson, A. Munkholm, M.V. Ramana Murty, O. Auciello, G.R. Bai, GB Stephenson, Observation of nanoscale 180° stripe domains in ferroelectric $PbTiO_3$ thin films, Phys. Rev. Lett. 89 (6) (2002), 067601.

[38] W.Y. Wang, Y.L. Zhu, Y.L. Tang, Y.B. Xu, Y. Liu, S. Li, S.R. Zhang, Y.J. Wang, X.L. Ma, Large scale arrays of four-state vortex domains in $BiFeO_3$ thin film, Appl. Phys. Lett. 109 (20) (2016) 202904.

[39] A.K. Tagantsev, G. Gerra, Interface-induced phenomena in polarization response of ferroelectric thin films, J. Appl. Phys. 100 (5) (2006), 051607.

[40] C. Kittel, Theory of the structure of ferromagnetic domains in films and small particles, Phys. Rev. 70 (11–12) (1946) 965–971.

[41] T. Mitsui, J. Furuichi, Domain structure of rochelle salt and KH_2PO_4, Phys. Rev. 90 (2) (1953) 193–202.

[42] G. Catalan, J. Seidel, R. Ramesh, J.F. Scott, Domain wall nanoelectronics, Rev. Mod. Phys. 84 (1) (2012) 119–156.

[43] M. Hÿtch, E. Snoeck, R. Kilaas, Quantitative measurement of displacement and strain fields from HREM micrographs, Ultramicroscopy 74 (3) (1998) 131–146.

[44] M.J. Hÿtch, J.L. Putaux, J. Thibault, Stress and strain around grain-boundary dislocations measured by high-resolution electron microscopy, Philos. Mag. A 86 (29–31) (2006) 4641–4656.

[45] M.J. Hÿtch, J.-L. Putaux, J.-M. Pénisson, Measurement of the displacement field of dislocations to 0.03 Å by electron microscopy, Nature 423 (6937) (2003) 270.

[46] S. Ducharme, V. Fridkin, A. Bune, S. Palto, L. Blinov, N. Petukhova, S. Yudin, Intrinsic ferroelectric coercive field, Phys. Rev. Lett. 84 (1) (2000) 175.